

# Efficient Bias Correction For MRI Image Denoising

Partha Sarathi Mukherjee<sup>1</sup> and Peihua Qiu<sup>2</sup>

<sup>1</sup>Department of Mathematics, Boise State University

<sup>2</sup>School of Statistics, University of Minnesota

## Abstract

Magnetic resonance imaging (MRI) is a popular radiology technique that is used for visualizing detailed internal structure of the body. Observed MRI images are generated by the inverse Fourier transformation from received frequency signals of a MR scanner system. Previous research has demonstrated that random noise involved in the observed MRI images can be described adequately by the so-called Rician noise model. Under that model, the observed image intensity at a given pixel is a non-linear function of the true image intensity and of two independent zero-mean random variables with a same normal distribution. Because of such a complicated noise structure in the observed MRI images, denoised images by conventional denoising methods are usually biased, and the bias could reduce image contrast and affect negatively subsequent image analysis. Therefore, it is important to address the bias issue properly. To this end, several bias correction procedures have been proposed in the literature. In this paper, we study the Rician noise model and the corresponding bias-correction problem systematically, and propose a new and more effective bias-correction formula based on the regression analysis and Monte Carlo simulation. Numerical studies show that our proposed method works well in various applications.

*Index Terms:* Bias correction, function approximation, image denoising, magnetic resonance imaging, medical imaging, Rician noise.

# 1 Introduction

Magnetic resonance imaging (MRI) is a technique that is used mainly for assessing pathological or other physiological conditions in living tissues, by visualizing the inside of living organisms [1]. In simple terms, its methodological basis lies in: (i) different tissues have different compositions and physical properties (e.g., water molecule densities) from which the tissue type at a given position can be determined, and (ii) these differences can be described by various image contrasts using the MRI technique.

When a part of a body (e.g., a patient's head) is placed in a uniform magnetic field of a given direction, say, the  $z$  direction, the hydrogen nuclei of water in that part of the body align themselves in parallel or anti-parallel with the field, creating a net magnetization, and rotate with the Larmor frequency. The basis of MRI lies in manipulating the local magnetic field such that the local resonant frequency would differ at different locations, which is achieved by applying additional, small, linear magnetic field gradients. In a MR scanner system, three orthogonally positioned gradient coils could produce such magnetic fields that vary linearly along their respective axes (e.g.,  $x$ ,  $y$ , and  $z$  axes), and these small fields are added to the main magnetic field. Turning on the coils in any particular combination would produce a field gradient along any desired direction. After applying radio frequency (RF) pulses transmitted by a separate RF coil, emitted radiation is absorbed by nuclei. Consequently, the net magnetization is tipped away from the main  $z$  axis; the nuclei continue their rotation, and as the excited nuclei relax back to the initial lower-energy alignment along the main field, RF signals are re-emitted and received by a RF receiver coil. Along the  $z$  direction, assume that a particular perpendicular slice of the body part at  $z = z_0$  is to be imaged. Then, a RF pulse with a frequency corresponding to that slice position could excite the nuclei in that plane. Considering only the proton density and spin relaxation, the received signal

can be expressed by

$$S(k_x, k_y) \propto \int \int_{\Omega_{z_0}} m(x, y) \exp[i2\pi(k_x x + k_y y)] dx dy, \quad (1)$$

where  $\Omega_{z_0}$  denotes the 2-dimensional (2-D) region of the slice,  $m(x, y)$  is the density of hydrogen protons at  $(x, y)$ ,  $k_x$  and  $k_y$  are the frequency change rates along the  $x$  and  $y$  directions of the local magnetic fields. Note that some constant multipliers have been ignored on the right-hand-side of (1) for simplicity. That is the reason why the “ $\propto$ ” symbol is used in the expression. From (1), it can be seen that  $S(k_x, k_y)$  is proportional to a Fourier transformation of  $m(x, y)$ . Therefore, if we have signals  $S(k_x, k_y)$  in the frequency domain, for all  $k_x, k_y = 1, 2, \dots, n$ , then  $m(x, y)$  can be determined in the spatial domain at  $n \times n$  regularly spaced pixels by the discrete inverse Fourier transformation [2, Chapter 7], as demonstrated in Figure 1.

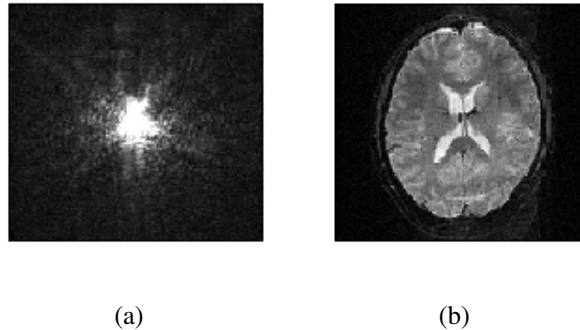


Figure 1: (a) Signals in frequency domain. (b) Corresponding spatial image obtained by the discrete inverse Fourier transformation of the signals shown in plot (a).

Note that equation (1) is only a theoretical model for describing the acquisition of MRI images. In practice, random noise is often involved in the received signal  $S(k_x, k_y)$  in the frequency domain, due to various reasons, including hardware imperfection, signal dropouts caused by field inhomogeneity, and so forth. In the literature, there is a considerable amount of existing research to describe the noise pattern in observed MRI images in the spatial domain (e.g., [3–4]). Most existing research shows that the noise pattern in observed MRI images can be described adequately

by the following Rician noise model (e.g., [5–6]):

$$Z(x, y) = \sqrt{[m(x, y) + N_1(x, y)]^2 + N_2^2(x, y)}, \quad (2)$$

where  $Z(x, y)$  denotes the observed image intensity at the pixel  $(x, y)$ ,  $m(x, y)$  is the true image intensity, and  $N_1(x, y)$  and  $N_2(x, y)$  are two independent random variables with the normal distribution  $N(0, \sigma^2)$  where  $\sigma$  is often unknown. One explanation of the Rician noise model (1) is that, when  $Z(x, y)$  is reconstructed from the frequency signal  $S(k_x, k_y)$  using the inverse Fourier transformation, the real part of the complex output of the transformation is  $m(x, y) + N_1(x, y)$ , the imaginary part is just the pure noise  $N_2(x, y)$  that does not contain any information about  $m(x, y)$ , and  $Z(x, y)$  is defined as the magnitude of the complex output of the inverse Fourier transformation (cf., [7]). This Rician noise model has been validated by some researchers using certain observed MR data (e.g., [8]).

From (2), we can see that the Rician noise involved in the observed image  $Z(x, y)$  does not have the traditional zero-mean and additive structure. Instead, its noise level depends on the true image intensity  $m(x, y)$ , and it contaminates  $m(x, y)$  nonlinearly. Because of the non-additivity and nonlinearity of the Rician noise, many conventional image denoising techniques, including the total variance minimization (e.g., [9]), anisotropic diffusion (e.g., [10]), non-local means (e.g., [11]), jump surface estimation (e.g., [12–13]), and so forth, would result in biased estimates of the true image intensity function  $m(x, y)$ , if they are applied directly to an observed MRI image with the Rician noise. A direct consequence is that the image contrast of these biased estimates would be lower than that of the true image (cf., [7]), because the magnitude of bias depends on the observed image intensities and the bias would be larger at places where the observed image intensities are smaller, which is unfavorable to subsequent image analysis.

In the literature, there are two types of existing methodologies to handle the image denoising

problem with the Rician noise. One is to estimate the true image intensity function  $m(x, y)$  directly from model (2), by exploring the functional relationship between  $m(x, y)$  and  $Z(x, y)$  (cf., [14–15]). For instance, Sijbers and den Dekker [16] suggested a denoising method based on the maximum likelihood estimation (MLE) of the true image  $m(x, y)$  in model (2). However, the MLE is not easy to obtain due to the nonlinearity of the model ([6]). Furthermore, this type of direct methods does not explicitly address the edge-preserving properties of the related estimators of  $m(x, y)$ ; thus, edges in the true image are not guaranteed to be preserved by them ([2], [6]). An alternative type of methods takes the following two-step approach (e.g., [3]). First, a conventional edge-preserving image denoising method is applied to an observed image with the Rician noise. Then, a bias-reduction procedure is used for post-processing the denoised image obtained in the first step to further improve the denoised image. By such a two-step approach, because edges are usually preserved in the first step and the bias-reduction in the second step is often accomplished by a continuous non-decreasing transformation (cf, the expression (8) below and the related discussion), edges are also preserved in the final estimator of the true image  $m(x, y)$ . Further, many conventional edge-preserving image denoising methods have been included in certain software packages. Therefore, the latter type of methods is convenient to use. For these reasons, the current paper focuses on the two-step approach to reduce bias of the denoised images by conventional image denoising methods in cases when the Rician noise is present.

In the literature, there are a number of existing bias-reduction methods for handling the Rician noise. For instance, Aja-Fernández et al. [17], Coupe et al. [18], Rajan et al. [19], and some others, recently proposed several different methods to estimate the noise level in an MRI image for reducing the bias caused by the Rician noise. Gudbjartsson and Patz [3] suggested the following bias-correction formula:

$$\hat{m}_1(x, y) = \sqrt{|\tilde{m}^2(x, y) - \sigma^2|}, \quad (3)$$

where  $\tilde{m}(x, y)$  denoted the denoised image by a conventional image denoising procedure (e.g., the non-local means method by Coupe et al. [20]), and  $\hat{m}_1(x, y)$  was the bias-corrected estimate of  $m(x, y)$ . The formula (3) was derived mainly using the normal distribution approximation to the Rician noise distribution. This distribution approximation may not be accurate in practice. Consequently, the accuracy of the formula (3) is in question as well. Wiest-Daessle et al. [21] noticed that  $E(Z^2(x, y)) = m^2(x, y) + 2\sigma^2$ , based on which they proposed the following bias-correction formula:

$$\hat{m}_2(x, y) = \sqrt{\tilde{m}^2(x, y) - 2\sigma^2} I\left(\tilde{m}(x, y) \geq \sqrt{2}\sigma\right), \quad (4)$$

where  $I(a)$  was an indicator function taking the value of 1 if “ $a=True$ ” and 0 otherwise. We have two reservations about the formula (4). First, in real applications, the cases when  $\tilde{m}(x, y) > \sqrt{2}\sigma$  can happen even in some pixels of the background region. By the formula (4),  $\hat{m}_2(x, y)$  is defined to be some positive number in all such cases, whereas it should be defined as 0. Second, the mathematical background of this formula is that  $E(Z^2(x, y)) = m^2(x, y) + 2\sigma^2$ . However, it is clear that we do not have the equality  $m(x, y) = \sqrt{[E(Z(x, y))]^2 - 2\sigma^2}$  in cases when  $m^2(x, y) = E(Z^2(x, y)) - 2\sigma^2$ . Therefore, this formula has room to be further improved.

In this paper, we propose a novel bias-correction method using the regression analysis and Monte Carlo simulation. From (2), it can be noticed that most conventional image denoising methods actually estimate  $E(Z(x, y))$ , instead of  $m(x, y)$ , because they are mainly based on data averaging for removing noise. The resulting bias is mainly contributed by  $E(Z(x, y)) - m(x, y)$  which is a function of  $m(x, y)$ . This function might be analytically complicated; but, it can be estimated accurately using the regression analysis and Monte Carlo simulation. Therefore, based on this idea, an accurate bias correction is possible.

The rest part of the article is organized as follows. The detail of our proposed method is de-

scribed in Section 2. Some numerical results are presented in Section 3. Several remarks conclude the article in Section 4.

## 2 Proposed Bias-Correction Method

In this section, we describe our proposed bias-correction method in details. First, the observed image intensity  $Z(x, y)$  at a given pixel  $(x, y)$  can always be decomposed into two parts: its mean  $E(Z(x, y))$  and the deviation from the mean  $Z(x, y) - E(Z(x, y))$ . In cases when the true image is contaminated by the Rician noise,  $Z(x, y)$  follows the model (2). In such cases, it can be written as

$$Z(x, y) = f(m(x, y)) + \varepsilon_m(x, y), \quad (5)$$

where  $f(m(x, y)) = E(Z(x, y))$  is the non-random mean part, and  $\varepsilon_m(x, y) = Z(x, y) - E(Z(x, y))$  is the zero-mean random part. It should be pointed out that, although it is not explicit in notation,  $f(m(x, y))$  and  $\varepsilon_m(x, y)$  may depend on the noise level  $\sigma$  and the true image intensity  $m(x, y)$ .

As discussed in Section 1, the denoised image  $\tilde{m}(x, y)$  by a conventional image denoising procedure from the observed image  $Z(x, y)$  is usually an asymptotically unbiased estimator of  $f(m(x, y))$  (cf., [2]), which would have an asymptotic bias of  $f(m(x, y)) - m(x, y)$  for estimating the true image  $m(x, y)$ . If the function  $f$  has an inverse  $g = f^{-1}$  and  $g$  can be properly specified, then a reasonable bias-corrected estimate of  $m(x, y)$  is

$$\hat{m}(x, y) = g(\tilde{m}(x, y)). \quad (6)$$

From models (2), we have

$$\frac{Z(x, y)}{\sigma} = \sqrt{\left[ \frac{m(x, y)}{\sigma} + \frac{N_1(x, y)}{\sigma} \right]^2 + \left[ \frac{N_2(x, y)}{\sigma} \right]^2},$$

where  $N_1(x, y)/\sigma$  and  $N_2(x, y)/\sigma$  are two random variables having the distribution  $N(0, 1)$ . Let  $f_1(m(x, y)/\sigma)$  be the mean of the term on the right-hand side of the above expression, and  $\varepsilon_{m,1}(x, y)$  be the deviation of this term from its mean. Then, we have

$$Z(x, y) = \sigma f_1\left(\frac{m(x, y)}{\sigma}\right) + \sigma \varepsilon_{m,1}(x, y).$$

Clearly,  $f_1(m(x, y)/\sigma)$  depends on  $m(x, y)/\sigma$  only. Since  $t = m(x, y)/\sigma$  can be interpreted as the signal-to-noise ratio (SNR),  $f_1$  can also be regarded as a function of SNR. Further, the above expression and expression (5) imply that  $f$  and  $g$  have the following properties:

$$f(t\sigma) = \sigma f_1(t), \quad g(s\sigma) = \sigma g_1(s), \quad (7)$$

where  $g_1$  denotes the inverse function of  $f_1$  (i.e.,  $g_1 = f_1^{-1}$ ), and  $s = f_1(t)$ . Note that these expressions are valid because  $f_1$  is a strictly increasing function (cf., Figure 2(a) below), thus  $f$  is a strictly increasing function as well, and therefore their inverse functions  $g_1$  and  $g$  both exist. By (6) and (7), if  $f_1$  or  $g_1$  can be properly specified, then the bias-corrected estimator of  $m(x, y)$  can be defined by

$$\hat{m}(x, y) = \hat{\sigma} g_1\left(\frac{\tilde{m}(x, y)}{\hat{\sigma}}\right), \quad (8)$$

where  $\hat{\sigma}$  is a reasonable estimate of  $\sigma$ . Intuitively,  $\tilde{m}(x, y)$  is asymptotically equal to  $E(Z(x, y)) = \sigma f_1(m(x, y)/\sigma)$ ; thus,  $\hat{m}(x, y)$  in (8) is asymptotically equal to  $\sigma g_1(f_1(m(x, y)/\sigma)) = m(x, y)$ . Therefore, this approach should work well, as long as  $\tilde{m}(x, y)$  and  $\hat{\sigma}$  estimate  $E(Z(x, y))$  and  $\sigma$  well.

The closed-form formulas of the functions  $f_1$  and  $g_1$  are difficult to derive. However, their expressions can be approximated accurately by a numerical approach described as follows. Let us first discuss the expression of  $f_1(t)$ . Because the image intensity of a real image is always non-negative, it is reasonable to constrain ourselves to  $t \geq 0$ . For a given  $t$ , we can generate  $\tilde{n}$

observed image intensity values by (2), in which  $m(x, y)$  is set to be  $t$  and  $N_1(x, y)$  and  $N_2(x, y)$  are replaced by two independent random numbers from the standard normal distribution. Then, by (5),  $f_1(t)$  can be estimated by the sample mean of the  $\tilde{n}$  observed image intensity values. When  $\tilde{n}$  is chosen large, such an estimate should be accurate by the strong law of large numbers (e.g., [22, Chapter 5]). For instance, when  $\tilde{n} = 10,000$  and  $t$  changes its values in  $[0, 10]$  with a step 0.01, the estimated  $f_1(t)$  is shown in Figure 2(a) by the dark solid line. From the plot, it can be seen that it is an increasing function when  $t \geq 0$ , and its value when  $t = 0$  can be easily computed to be 1.253. As a reference, the light solid line in the plot denotes the identity transformation. As described above, a conventional image denoising procedure has an asymptotic bias of  $f(m(x, y)) - m(x, y) = \sigma[f_1(t) - t]$ . Therefore, from Figure 2(a), it can be seen that (i) the conventional image denoising procedure would have positive biases across the entire image, and (ii) the biases is larger at places with smaller SNR values.

The estimated  $g_1(s)$ , which is obtained from the estimated  $f_1(t)$  shown in Figure 2(a) by switching the  $x$  and  $y$  axes, is shown in Figure 2(b) by the dark solid line. As a comparison, in the case when  $\sigma = 1$ , the corresponding transformations of the bias correction formulas (3) and (4) described in Section 1, suggested by Gudbjartsson and Patz [3] and Wiest-Daessle et al. [21], respectively, are  $\sqrt{|s^2 - 1|}$  and  $\sqrt{s^2 - 2}I(s \geq \sqrt{2})$ . They are also displayed in the same plot by the long-dashed and short-dashed lines, respectively. From the plot, we can see that all three bias correction methods try to pull down the estimated image intensities of a conventional image denoising procedure. However, compared to the proposed formula (8), the formula (3) seems not to correct the bias big enough especially when  $s \leq 1$ , while the formula (4) seems to over-correct the bias.

In practice, we need to obtain a good estimator  $\hat{\sigma}$  of  $\sigma$  before we can use formula (8) for bias correction. To this end, one simple method is to use the sample variance of  $Z^2(x, y)$  in the back-

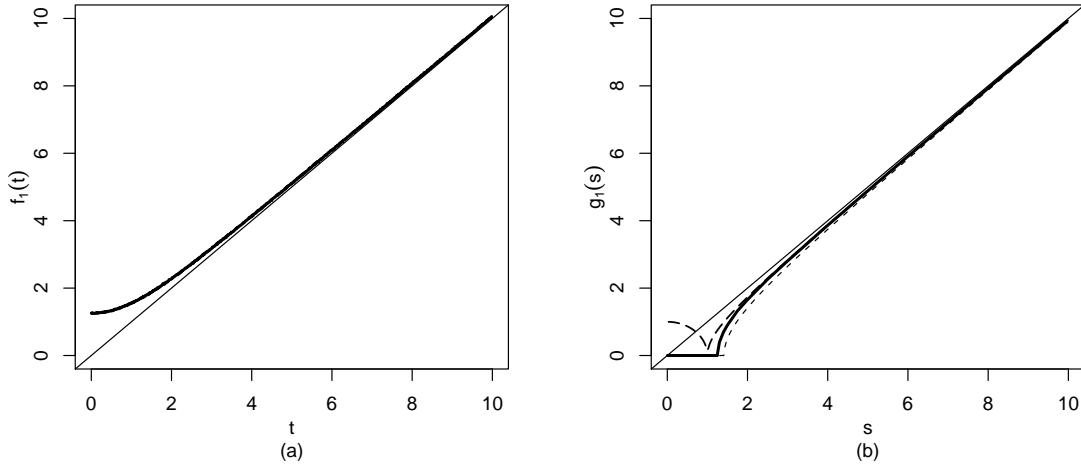


Figure 2: (a) Function  $f_1(t)$  (dark solid line) estimated by simulation, and the identity transformation (light solid line). (b) Transformation function  $g_1(s)$  in the proposed bias correction formula (8) (dark solid line), the corresponding transformation functions of the formulas (3) and (4) (long-dashed and short-dashed lines, respectively), and the identity transformation (light solid line).

ground region of an MRI image, because  $m(x, y)$  is close to zero in the background and thus the sample variance of  $Z^2(x, y)$  in that region would be approximately  $4\sigma^4$ . In the literature, there are a few alternative methods for estimating  $\sigma$  (e.g., [17–19]); but these methods are more computationally extensive. We checked the numerical performance of our proposed bias-correction method, and found that its performance using the simple estimator  $\hat{\sigma}$  described above is similar to its performance when we pretend that  $\sigma$  is known.

After  $\hat{\sigma}$  is obtained, we can compute the value of  $g_1(s)$  with  $s = \tilde{m}(x, y)/\hat{\sigma}$  by an algorithm similar to the one described above for creating Figure 2(b), after  $\tilde{m}(x, y)$  is computed by a conventional image denoising procedure. However, if we can derive an explicit formula that provides a good approximation to the transformation function  $g_1(s)$ , then the use of our proposed bias correction formula (8) will be greatly simplified. To this end, we suggest approximating  $g_1(s)$  by the

first-order regression spline function

$$\beta_{-1} + \beta_0 s + \sum_{j=1}^{\ell} \beta_j (s - v_j)_+,$$

where  $\boldsymbol{\beta} = (\beta_{-1}, \beta_0, \beta_1, \dots, \beta_{\ell})$  are coefficients,  $(1, s, (s - v_1)_+, \dots, (s - v_{\ell})_+)$  are the basis functions,  $(s - v)_+ = (s - v)$  if  $s \geq v$  and 0 otherwise, and  $(v_1, v_2, \dots, v_{\ell})$  are the set of selected knots.

From Figure 2(b), it can be seen that  $g_1(s)$  is almost straight when  $s > 2$ , and it is curved mainly in cases when  $s \in [1.253, 2]$ . Therefore, the selected knots should be dense in the region  $[1.253, 2]$ , and relatively sparse in the region when  $s > 2$ . Also, our numerical study shows that  $g_1(s)$  can be simply approximated by  $s$  when  $s > 10$ , without losing any meaningful approximation accuracy. So, we constrain ourselves to cases when  $s \in [0, 10]$ . Based on all these considerations and an extensive numerical study, we choose the following set of knots:

$$(1.253, 1.3, 1.4, 1.5, 1.75, 2.0, 2.5, 3.0, 4.0, 5.0, 6.0, 7.0, 8.0, 9.0, 10.0).$$

To estimate the above regression spline function in  $[0, 10]$ , we generate the data in the same way as we compute the estimated values of  $g_1(s)$  shown in Figure 2(b), and the estimated values of  $g_1(s)$  are used as the observed data of the response variable here. Then, the regression spline approximation, denoted as  $\hat{g}_{S,1}(s)$ , has the expression

$$\hat{g}_{S,1}(s) = \hat{\beta}_{-1} + \hat{\beta}_0 s + \sum_{j=1}^{\ell} \hat{\beta}_j (s - v_j)_+$$

where  $\hat{\boldsymbol{\beta}} = (\hat{\beta}_{-1}, \hat{\beta}_0, \hat{\beta}_1, \dots, \hat{\beta}_{\ell})$  is the least squares estimate of  $\boldsymbol{\beta}$ .

With the knots specified above, the MSE of  $\hat{g}_{S,1}$  in approximating  $g_1$ , defined to be

$$MSE = \frac{1}{1000} \sum_{i=1}^{1000} \left[ \hat{g}_{S,1} \left( 1.253 + \frac{i(10 - 1.253)}{1000} \right) - g_1 \left( 1.253 + \frac{i(10 - 1.253)}{1000} \right) \right]^2,$$

is  $2.273 \times 10^{-4}$ , where the function  $g_1$  is the one shown in Figure 2(b). When choosing the knots, we actually performed extensive simulations with many different sets of finer knots. With a set

of finer knots, the improvement in the MSE is typically smaller than  $10^{-6}$ , and the improvement in the MISE of the bias-corrected denoised image  $\widehat{m}(x, y)$  in (8) (see the definition of MISE in Section 3) is typically smaller than one-fifth of the standard error of the MISE. For these reasons, we think that the set of knots specified above is good enough for applications, and it is used in all numerical examples in Section 3.

In the formula (4) suggested by Wiest-Daessle et al. [21], a threshold value  $\sqrt{2}$  is used for the ratio  $\widetilde{m}(x, y)/\sigma$ . In cases when  $\widetilde{m}(x, y)/\sigma < \sqrt{2}$ , that formula simply defines the corrected image intensity to be 0. We have studied the legitimacy of the inclusion of such a threshold value in our research, and found that the threshold value is indeed necessary, for the following reason. In a typical MRI image, pixels with lower SNR values are usually located in the background regions, and it is thus reasonable to set the corrected image intensities at such pixels to be 0. We performed many numerical studies, and found that inclusion of a threshold value  $T$  in the range of  $[\sqrt{2}, 1.5]$  would generally improve the quality of the bias-corrected MRI images (see numerical results reported in Section 3). From Figure 2(b), “ $T = \sqrt{2}$ ” corresponds to the corrected SNR  $\widehat{m}(x, y)/\sigma$  of about 0.7, and “ $T = 1.5$ ” corresponds to the corrected SNR of about 0.9. Based on all the considerations described above, we suggest using the following formula for approximating  $g_1(s)$ :

$$\widehat{g}_1(s) = \begin{cases} 0, & \text{when } s < T \\ \widehat{g}_{s,1}(s), & \text{when } T \leq s \leq 10 \\ s, & \text{when } s > 10, \end{cases} \quad (9)$$

where  $T$  is a threshold value. Then, by our proposed approach, bias correction of the denoised image  $\widetilde{m}(x, y)$  of a conventional image denoising procedure can be accomplished by using (8), after  $g_1$  is replaced by  $\widehat{g}_1$  defined in (9).

### 3 Numerical Studies

In this section, we present some numerical examples to investigate the performance of our proposed bias-correction formulas (8)-(9), denoted as NEW, in comparison with two commonly used bias-correction methods in practice: the normal approximation formula (3), denoted as GP, and the moment-based formula (4), denoted as WD. Both formulas (3) and (4) are described in Section 1. The performance of all three bias-correction methods is evaluated using three popular conventional image denoising methods: the total variance (TV) procedure by Rudin et al. [9], the anisotropic diffusion (AD) procedure by Perona and Malik [10], and the optimized non-local means (ONLM) algorithm by Coupe et al. [20]. For TV and AD, the MATLAB codes presented by Getreuer [23] and Lopes [24] are used. To evaluate the performance of a bias-correction method, we use the standard criterion of the estimated mean integrated squared error (MISE), defined as follows. Let  $m(x, y)$  be the true image and  $\widehat{m}(x, y)$  be the bias-corrected estimate of  $m(x, y)$ . Then, the integrated squared error is estimated by

$$\text{ISE} = \frac{1}{N} \sum_{(x,y)} [\widehat{m}(x, y) - m(x, y)]^2,$$

where  $N$  denotes the total number of pixels and  $\sum_{(x,y)}$  denotes the summation over all pixels. Then, the MISE is estimated by the sample mean of the 100 ISE values computed from 100 replicated simulations. By this criterion, the bias-correction method performs better if its MISE value is smaller. The MISE value provides a measure of the overall performance of the denoised image  $\widehat{m}(x, y)$  for estimating the true image  $m(x, y)$ . For comparing different bias-correction methods, it is also natural to consider the criterion

$$\text{ABIAS} = \frac{1}{N} \sum_{(x,y)} \left| \widehat{m}(x, y) - m(x, y) \right|,$$

where  $\widehat{m}(x, y)$  is the sample mean of 100  $\widehat{m}(x, y)$  values computed from 100 replications. Because  $\widehat{m}(x, y)$  is an estimate of  $E(\widehat{m}(x, y))$ , ABIAS is just the averaged absolute bias of the denoised image  $\widehat{m}(x, y)$  for estimating the true image  $m(x, y)$ . Note that the absolute bias  $|\widehat{m}(x, y) - m(x, y)|$ , instead of just the bias  $(\widehat{m}(x, y) - m(x, y))$ , is used in the above definition of ABIAS to avoid cancellation of positive and negative biases at different places of the image. In the bias-correction literature, another popular criterion is the “contrast” of an image, defined to be the difference between the intensities of the brightest and the darkest pixels (cf., [20]). The rationale of this criterion is that the estimation bias caused by the Rician noise would decrease the image contrast. So, by this criterion, a bias-correction method performs better if the contrast of its bias-corrected image is larger. However, the contrast defined above is sensitive to outliers. To make it more robust to outliers, in this paper, we use the trimmed contrast, defined to be the contrast of an image, after its 1% largest and 1% smallest intensities are removed.

We first use two MRI images of a brain and an ankle as test images. The brain image has  $350 \times 350$  pixels, and the ankle image has  $432 \times 432$  pixels. In both images, the intensity values range from 0 to 255. We then add the Rician noise of two different levels  $\sigma = 40$  and  $\sigma = 60$  to the test images (cf., model (2)). The true and noisy test images are presented in Figures 3 and 4.

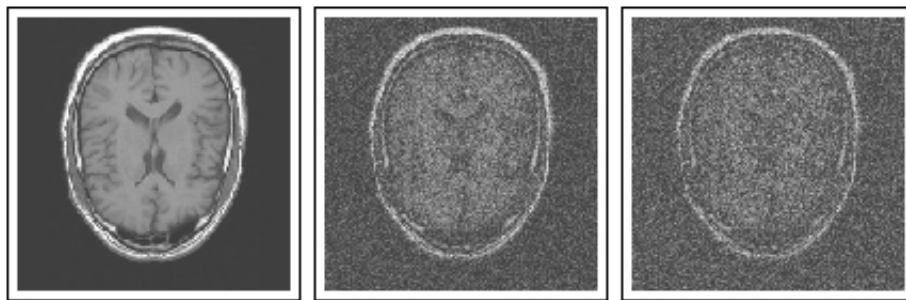


Figure 3: The true brain test image and its two noisy versions with  $\sigma = 40$  and 60.

We then apply the denoising methods TV, AD, and ONLM to various test images, and then



Figure 4: The true ankle test image and its two noisy versions with  $\sigma = 40$  and  $60$ .

use the bias-correction methods NEW, GP, and WD to correct biases of the denoised images. When using the method NEW, the noise level estimate  $\hat{\sigma}$  used in (8) is computed using the method described in Section 2, based on the first  $[1, 32] \times [1, 32]$  pixels of each image which should be all in background regions. We tried several different background regions for computing  $\hat{\sigma}$ , and found that  $\hat{\sigma}$  is not sensitive to the choice of the background regions. In the procedures GP and WD, a similar estimate to  $\hat{\sigma}$  is obtained from a background region, and is used in the bias-correction formulas (3) and (4). For each pair of the denoising and bias-correction methods, the procedure parameters are chosen to minimize the estimated MISE value of the bias-corrected image. For the method NEW, four values of the threshold  $T$  are considered (cf., formula (9)). They are 1.253,  $\sqrt{2}$ , 1.5, and 1.55. The four versions with these four threshold values are denoted as NEW1, NEW2, NEW3, and NEW4, respectively. The estimated MISE values and their standard errors, the estimated ABIAS values, and the sample mean values of the trimmed contrasts and their standard errors are presented in Tables 1 and 2. To compare two methods with respect to the performance measure MISE, if their estimated values of MISE are  $MISE_1$  and  $MISE_2$  with standard errors  $SE_1$  and  $SE_2$ , respectively, and  $MISE_1 < MISE_2$ , then a practical guideline commonly used in practice is that we can conclude that the method 1 is significantly better than the method 2 in cases when  $MISE_2 - MISE_1 > \nu(SE_1 + SE_2)$ , where  $\nu > 0$  is a given number. In practice, people often

choose  $\nu$  from the interval  $[1, 2]$ . We can make similar comparisons using the standard errors of the estimated trimmed contrasts.

From Table 1, we can have the following conclusions. First, the bias-correction procedure NEW3 is better than its peers GP and WD in all cases in terms of the MISE criterion. Second, the bias-correction procedures NEW2, NEW3, and NEW4 are better than its peers GP and WD in all cases in terms of the ABIAS criterion. Third, all four versions of NEW are better than GP and WD in all cases in terms of the trimmed contrast. Fourth, NEW2 and NEW3 are generally better than NEW1 and NEW4, and it seems that, NEW3 is slightly better when the noise level is relatively low (i.e.,  $\sigma = 40$ ), and NEW2 is slightly better when the noise level is relatively high (i.e.,  $\sigma = 60$ ) except the case with AD in terms of MISE. Similar conclusions can be obtained from the results in Table 2.

As discussed in Section 2, the function  $g_1(s)$  is defined in the interval  $[1.253, \infty)$  (cf., Figure 2(b)). So, the version NEW1, in which  $T = 1.253$ , is the same as the proposed method NEW without using the threshold value  $T$  (cf., the definition of  $\hat{g}_1(s)$  in (9)). From the results in Tables 1 and 2, it seems that it helps by using the threshold value  $T$ , since NEW2, NEW3 and NEW4 are better than NEW1 in all cases considered, except the case when  $\sigma = 60$  in Table 2 where NEW4 is worse than NEW1 in terms of MISE and the trimmed contrast. As pointed out in the paragraph containing the expression (9) in Section 2, the main purpose to use the threshold value  $T$  is for handling pixels in the background. When the estimated SNR at a given pixel is low, the pixel is most probably a background pixel and thus it is reasonable to set its bias-corrected image intensity to be 0. When  $T$  is chosen large, it is possible that many foreground pixels would be mistakenly treated as background pixels. On the other hand, when  $T$  is chosen small, it is possible that many background pixels would be treated as foreground pixels and receive positive intensity values after bias-correction. It is easy to check that the corresponding threshold values on the estimated SNR

Table 1: Performance of the methods in the brain image example. In each cell, the first row presents the estimated MISE value and its standard error (in parenthesis), the second row presents the estimated ABIAS value, and the third row presents the estimated trimmed contrast and its standard error. All results are based on 100 random simulations.

Method	$\sigma = 40$			$\sigma = 60$		
	TV	AD	ONLM	TV	AD	ONLM
GP	607.7 (37.4)	608.0 (30.9)	592.7 (34.1)	1354.0 (95.0)	1312.0 (87.9)	1305.1 (81.6)
	20.0	19.3	19.2	30.5	29.0	29.1
	204.5 (1.7)	217.3 (1.6)	224.2 (2.0)	182.6 (2.8)	199.3 (2.6)	212.2 (3.2)
WD	161.4 (6.5)	179.7 (3.7)	172.5 (5.2)	327.8 (26.1)	380.6 (28.1)	373.0 (29.8)
	6.4	6.3	6.1	10.2	10.2	10.0
	224.2 (1.1)	224.8 (1.0)	234.5 (1.0)	210.6 (1.8)	207.2 (1.6)	227.3 (1.8)
NEW1	203.2 (38.9)	249.7 (31.9)	228.5 (32.2)	366.0 (75.6)	469.7 (70.4)	441.7 (74.6)
	7.9	8.6	8.2	11.4	12.1	11.7
	227.5 (1.0)	227.7 (1.0)	237.6 (1.0)	218.1 (1.6)	215.1 (1.4)	234.4 (1.6)
NEW2	152.4 (5.5)	197.6 (23.3)	173.7 (15.4)	271.3 (23.4)	360.4 (34.9)	328.4 (28.1)
	5.2	5.3	4.8	7.1	6.8	6.4
	227.6 (1.1)	228.1 (1.0)	237.6 (1.0)	218.3 (1.7)	214.8 (1.5)	234.4 (1.6)
NEW3	149.9 (2.3)	171.4 (9.0)	162.0 (4.3)	275.8 (12.0)	341.6 (11.4)	339.9 (16.4)
	5.1	4.9	4.7	7.0	6.2	6.5
	227.4 (1.0)	227.9 (0.9)	237.5 (1.0)	217.9 (1.6)	214.7 (1.4)	234.2 (1.7)
NEW4	151.6 (2.4)	167.6 (3.5)	164.1 (3.4)	297.4 (20.9)	359.2 (17.0)	376.4 (29.3)
	5.1	4.9	4.7	7.1	6.6	6.8
	227.5 (1.0)	227.9 (1.0)	237.6 (1.0)	218.2 (1.6)	215.0 (1.4)	234.4 (1.6)

Table 2: Performance of the methods in the ankle image example. In each cell, the first row presents the estimated MISE value and its standard error (in parenthesis), the second row presents the estimated ABIAS value, and the third row presents the estimated trimmed contrast and its standard error. All results are based on 100 random simulations.

Method	$\sigma = 40$			$\sigma = 60$		
	TV	AD	ONLM	TV	AD	ONLM
GP	531.9 (33.8)	540.9 (30.2)	538.8 (27.0)	1166.5 (81.3)	1166.9 (72.2)	1162.4 (67.2)
	18.4	18.6	18.7	28.6	28.2	28.1
	219.4 (2.0)	231.3 (1.9)	228.5 (1.7)	202.5 (2.4)	220.0 (2.4)	217.1 (2.8)
WD	198.9 (8.0)	215.0 (5.3)	222.7 (6.2)	381.1 (47.1)	410.4 (29.1)	433.2 (35.3)
	7.7	8.1	8.4	11.3	11.8	12.0
	238.6 (0.8)	238.4 (0.7)	238.7 (0.8)	231.0 (1.2)	231.8 (1.1)	233.1 (1.3)
NEW1	218.5 (26.0)	257.5 (22.3)	252.3 (21.5)	352.5 (55.1)	462.9 (55.2)	439.0 (53.0)
	8.1	9.2	8.9	11.0	12.1	12.0
	241.5 (0.8)	241.7 (0.7)	241.7 (0.8)	238.1 (1.0)	239.0 (0.8)	240.1 (1.2)
NEW2	187.7 (6.5)	229.5 (16.2)	221.0 (10.2)	297.8 (10.6)	390.1 (24.8)	380.2 (13.9)
	6.8	7.3	7.4	8.7	9.2	9.3
	241.8 (0.6)	241.6 (0.6)	241.7 (0.8)	238.2 (1.1)	239.0 (0.8)	240.1 (1.2)
NEW3	188.2 (2.2)	211.1 (6.7)	214.1 (2.9)	335.7 (25.7)	409.9 (18.7)	428.7 (30.9)
	6.8	7.3	7.5	9.0	9.8	10.0
	241.5 (0.7)	241.4 (0.6)	241.7 (0.8)	237.8 (1.0)	238.7 (0.9)	239.9 (1.2)
NEW4	192.8 (4.0)	210.5 (4.3)	217.3 (3.6)	401.5 (53.2)	464.0 (43.3)	495.1 (47.4)
	6.9	7.4	7.6	9.8	10.4	10.9
	241.7 (0.7)	241.6 (0.6)	241.7 (0.8)	238.0 (1.1)	238.9 (0.8)	240.1 (1.2)

are 0, 0.7, 0.9, and 1 in cases when  $T = 1.253, \sqrt{2}, 1.5,$  and  $1.55$ . In our numerical studies, we actually tried many other values of  $T$ . In all the examples considered, we found that the results always got worse than those of NEW4 when  $T$  was chosen larger than 1.55, and the results were between those of NEW1 and NEW2 when  $T$  was chosen between 1.253 and  $\sqrt{2}$ . Based on these results and the results in Tables 1 and 2, it seems that the results are reasonably good when  $T$  is chosen in the range  $[\sqrt{2}, 1.5]$ . In cases when the noise level is low,  $T$  should be chosen close to the right end of this interval, and it should be chosen close to the left end of the interval when the noise level is high. In cases when we are not sure about the noise level in a specific application, we suggest choosing  $T = 1.5$ , which is used in all examples below. From these examples, it can be seen that our proposed method using this  $T$  value performs well.

The bias-corrected denoised images of the noisy brain image with  $\sigma = 40$  (cf., the middle panel in Figure 3) are shown in Figure 5, in which rows 1–3 present the denoised images by TV, AD and ONLM, and columns 1–3 present the bias-corrected denoised images by GP, WD and NEW3. Row 4 shows the deviation images defined to be (bias-corrected denoised image - true image) by the denoising procedure TV and by the bias-correction procedures GP, WD and NEW3, respectively. From the bias-corrected denoised images, it can be seen that the ones corrected by NEW3 are slightly sharper than the others. The deviation images show that the bias-corrected denoised image by NEW3 has the smallest deviation, compared to the images corrected by the other two procedures, although the difference between the second and the third images is small. Figure 6 shows the corresponding results for the ankle test image. Similar conclusions to those described above can be made from the results shown in Figure 6.

In the above example, the Rician noise is assumed to have a constant noise level in an entire observed image. In practice, the noise level may change spatially. Next, we consider a case when the Rician noise with a variable level is added to the ankle image, and the variable noise level is

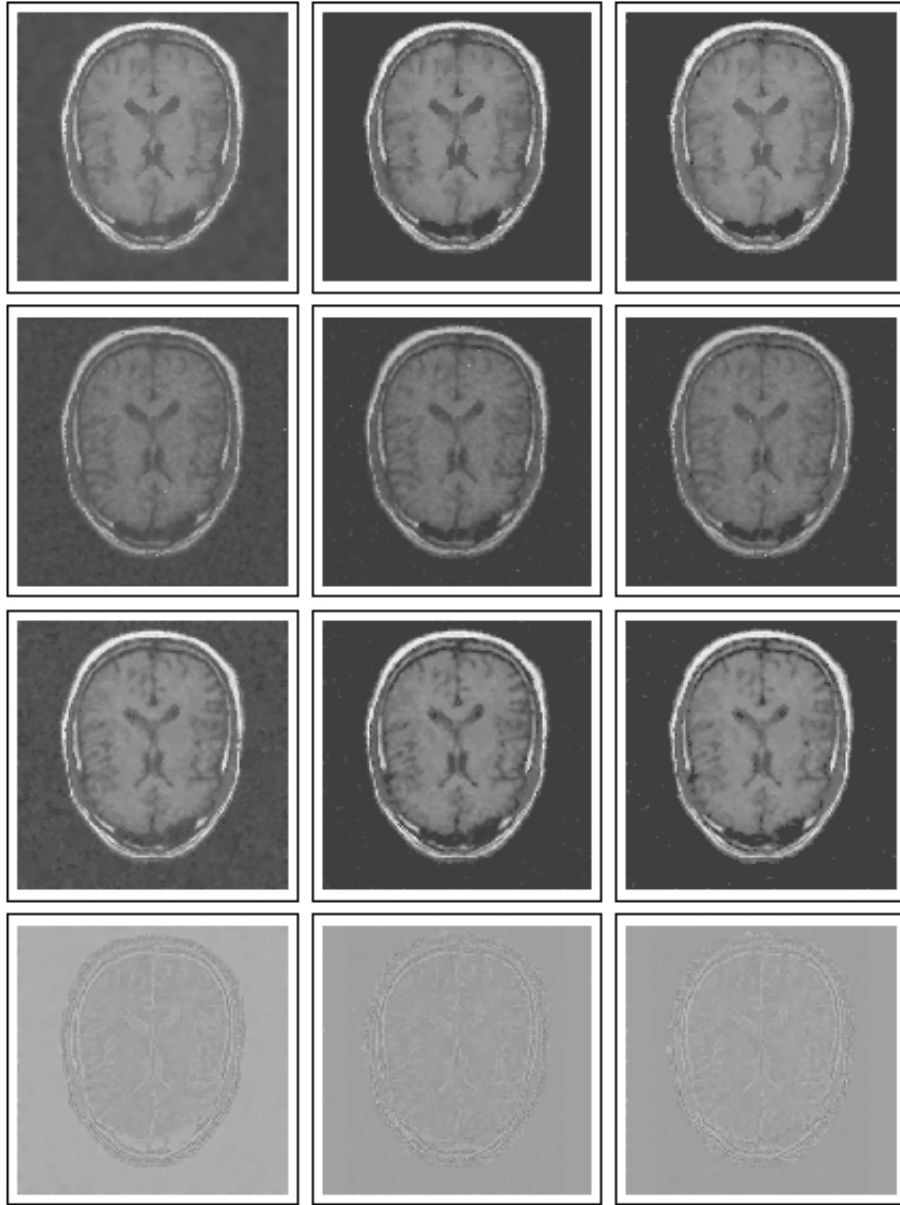


Figure 5: Bias-corrected denoised images in the brain image example with  $\sigma = 40$ . Rows 1-3 presents the denoised images by denoising procedures TV, AD and ONLM. Columns 1-3 presents the bias-corrected denoised images by procedures GP, WD and NEW3. Row 4 shows the bias images defined to be (bias-corrected denoised image - true image) by the denoising procedure TV and by the bias-correction procedures GP, WD and NEW3, respectively.

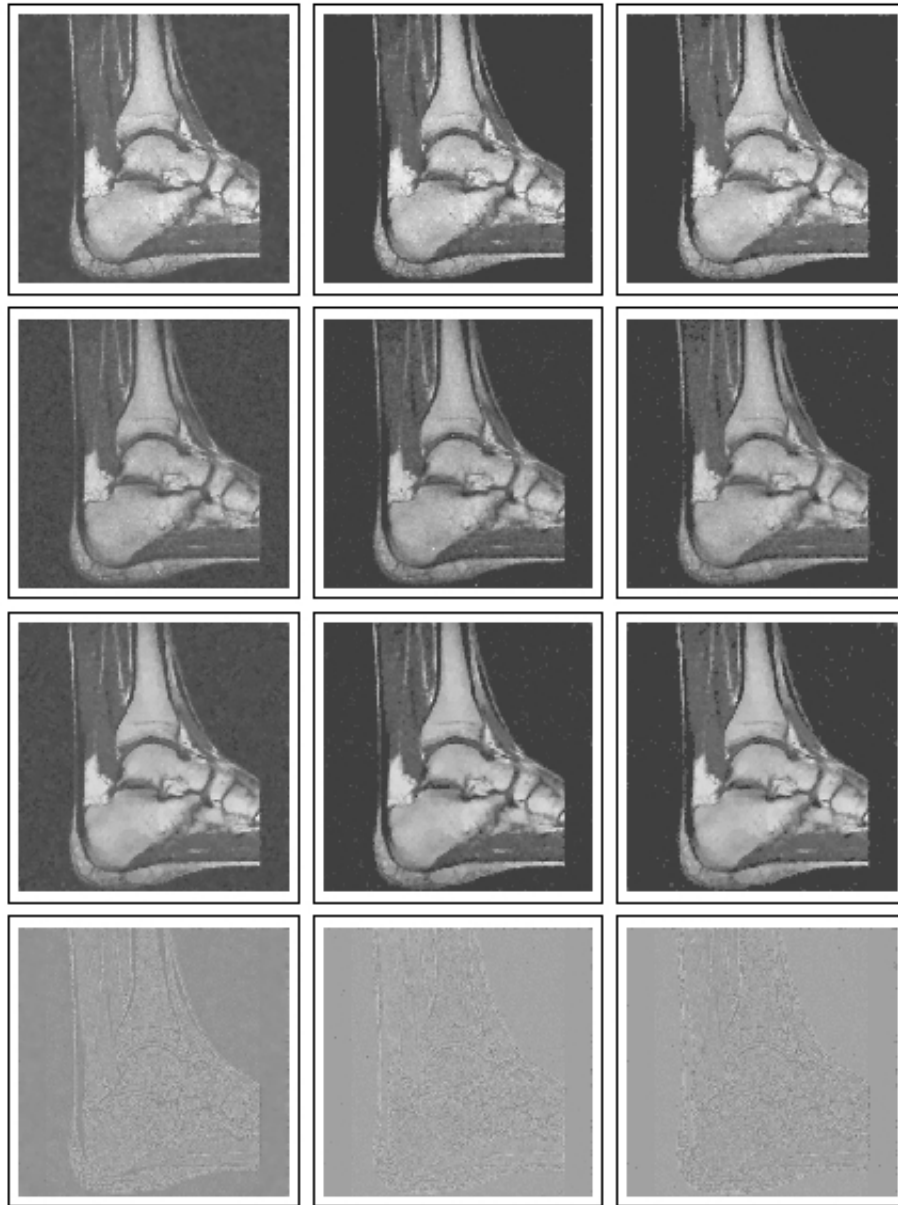


Figure 6: Bias-corrected denoised images in the ankle image example with  $\sigma = 40$ . Rows 1-3 presents the denoised images by denoising procedures TV, AD and ONLM. Columns 1-3 presents the bias-corrected denoised images by procedures GP, WD and NEW3. Row 4 shows the bias images defined to be (bias-corrected denoised image - true image) by the denoising procedure TV and by the bias-correction procedures GP, WD and NEW3, respectively.

specified by

$$\sigma(x, y) = 20 + 40 \exp \left( -(x - 0.5)^2/4 - (y - 0.5)^2/4 \right).$$

One noisy ankle image with this variable noise level is shown in the left panel of Figure 7, and the three bias-corrected versions by GP, WD, and NEW3 of the denoised image by TV are shown by the three images in the first row of Figure 8, respectively. The deviation images of the three bias-corrected versions are shown in the second row of Figure 8. From these images, it can be seen that the bias-corrected image by NEW3 is sharper than the other two bias-corrected images, and the pattern in its deviation image seems to be weaker than those in the other two deviation images. The estimated MISE values and their standard errors, the estimated ABIAS values, and the estimated trimmed contrasts and their standard errors, based on 100 replications, are presented in the upper part of Table 3. From the table, it can be seen that NEW3 is better than GP and WD in this case by all three performance evaluation criteria.

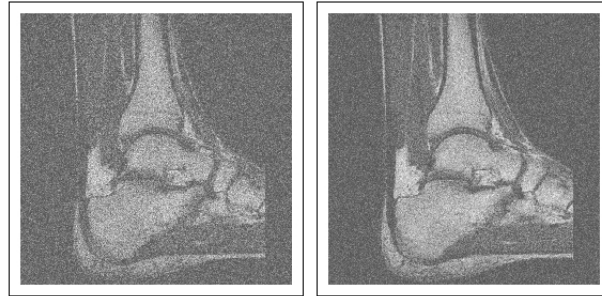


Figure 7: The left panel shows a noisy version of the ankle test image with a variable noise level across the image, and the right panel shows another noisy version of the same test image with spatially correlated Rician noise.

In all the above examples, the Rician noise is assumed independent at different pixels. In practice, the Rician noise might be spatially correlated. In such cases, the expression (2) still holds, except that  $N_1(x, y)$  and  $N_2(x, y)$  might be spatially correlated. It can be checked that all

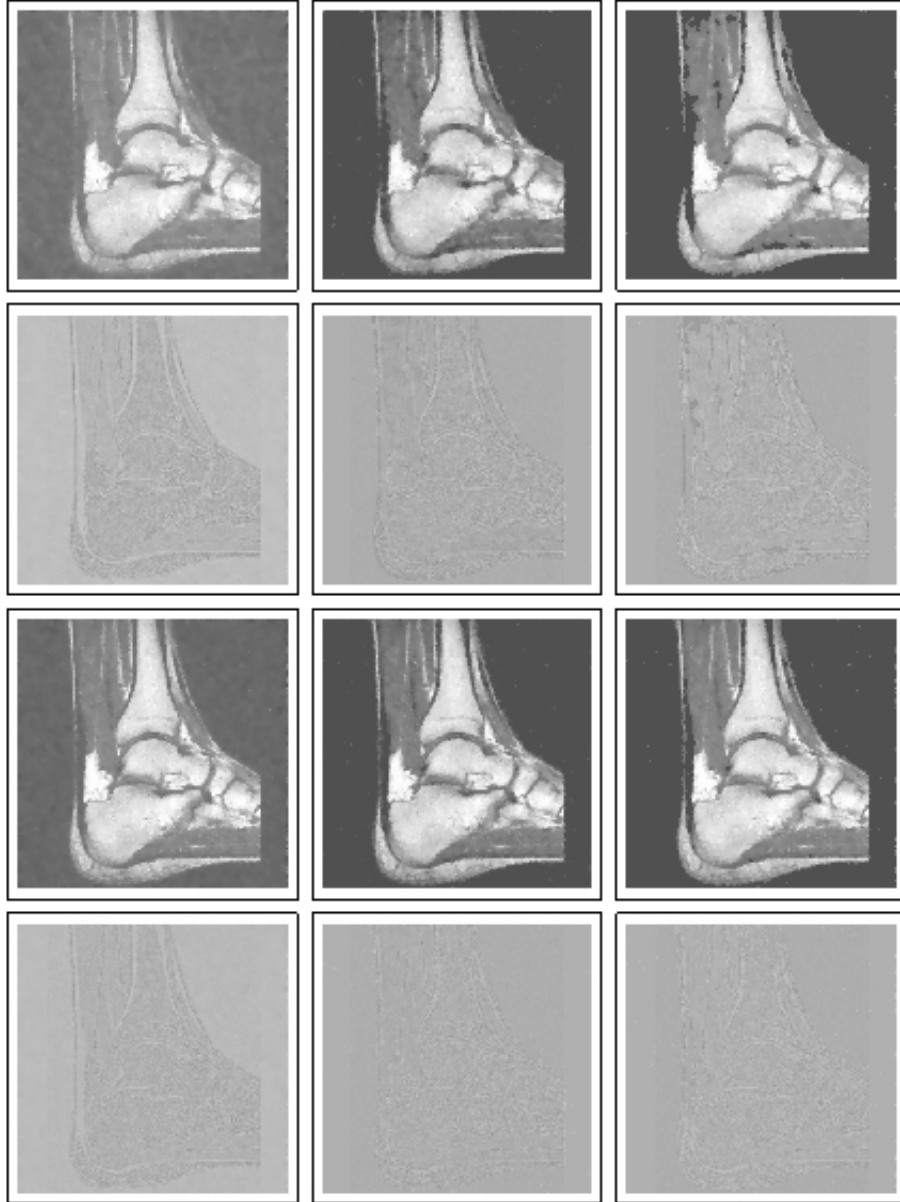


Figure 8: Images in the first row show the three bias-corrected versions by GP, WD, and NEW3 of the denoised image by TV in cases when the observed image is the one shown in the left panel of Figure 7 with variable noise level. Images in the second row show the corresponding deviation images. Images in the third and fourth rows are the corresponding results in cases when the observed image is the one shown in the right panel of Figure 7 with spatially correlated Rician noise.

Table 3: Performance of the bias-correction methods GP, WD, and NEW3 in the ankle image example, in cases when the noise level is spatially variable and when the noise is spatially correlated. In each cell, the first row presents the estimated MISE value and its standard error (in parenthesis), the second row presents the estimated ABIAS value, and the third row presents the estimated trimmed contrast and its standard error. All results are based on 100 random simulations.

	GP	WD	NEW3
Variable $\sigma$	1192.0 (73.2)	305.0 (17.3)	303.9 (6.0)
	28.8	9.5	8.5
	205.2 (1.9)	234.6 (1.1)	240.3 (1.0)
Correlated noise	536.0 (28.3)	199.9 (7.7)	187.9 (2.3)
	18.6	7.7	6.8
	219.1 (1.8)	238.5 (0.8)	241.6 (0.7)

arguments about our proposed bias-correction method given in Section 2 are valid in this case. Therefore, we expect our method still performs well. To confirm this, in the next example, we consider adding spatially correlated Rician noise to the ankle test image, and investigating the performance of our proposed method which does not take into account such a spatial correlation in its construction. The spatial correlation in the Rician noise is described as follows. In model (2), we assume that for any pixel  $(x, y)$ ,

$$\text{Cov}(N_1(x, y), N_1(x', y')) = \begin{cases} 40^2 & \text{if } (x, y) = (x', y') \\ 0.8 \times 40^2 & \text{if } |x - x'| = 1 \text{ or } |y - y'| = 1 \\ 0 & \text{otherwise.} \end{cases}$$

Namely,  $N_1(x, y)$  is spatially correlated with the corresponding noise at the four closest pixels of

$(x, y)$ , and independent of the noise at other pixels. The spatial correlation structure of  $N_2(x, y)$  is assumed the same as that of  $N_1(x, y)$ . One observed noisy test image is shown in the right panel of Figure 7, the three bias-corrected versions by GP, WD, and NEW3 of the denoised image by TV are shown by the three images in the third row of Figure 8, respectively, and the deviation images of the three bias-corrected versions are shown in the fourth row of Figure 8. Again, the bias-corrected image by NEW3 looks sharper than the other two bias-corrected images, and the pattern in its deviation image seems weaker than those in the other two deviation images. The estimated MISE values and their standard errors, the estimated ABIAS values, and the estimated trimmed contrasts and their standard errors, based on 100 replications, are presented in the lower part of Table 3. From the table, it can be seen that NEW3 is better than GP and WD in this case by all three evaluation criteria as well.

Next, we consider a real noisy MRI image shown in Figure 9, which was also used by Marjón et al. [25]. This image has  $205 \times 205$  pixels with the image intensities in the range  $[0, 255]$ . In this case, because the true image is unknown, the MISE and ABIAS criteria cannot be used here and the trimmed contrast is the only criterion that we can compute. For the three bias-correction methods GP, WD, and NEW3, their parameters are chosen to maximize the trimmed contrast. The results of their trimmed contrasts are summarized in Table 4. From the table, it can be seen that NEW3 is better than GP and WD in all cases. Their bias-corrected denoised images are shown in Figure 10.

Since we do not know the ground truth of a real MRI image, it is difficult to make thorough comparisons among the competing methods. Next, we downloaded a noiseless T1-weighted 3-D brain phantom image from the BrainWeb database ([26–30]) with 40% intensity non-uniformity, and considered one slice of that image for the purpose of comparisons. We consider intensity non-uniformity here because it is more realistic ([26–30]). Literature ([20], [26–30]) showed that

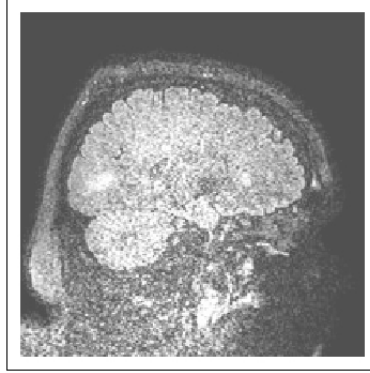


Figure 9: A real noisy MRI image with  $205 \times 205$  pixels.

Table 4: Estimated trimmed contrasts of the bias-correction methods GP, WD, and NEW3 in the real noisy MRI image example.

	GP	WD	NEW3
TV	212.9	218.2	220.2
AD	224.3	229.8	231.7
ONLM	225.2	231.0	233.0

0% – 9% Rician noise was common in real applications, although sometimes it was reasonable to assume the noise to be as high as about 20% ([20]). By  $x\%$  Rician noise we mean  $\sigma$  is  $x\%$  of the image contrast. In our simulations, we considered 3%, 5%, 9% and 20% Rician noise. The selected slice of the noiseless phantom and its noisy versions are shown in Figure 11. This slice contains  $217 \times 181$  pixels, and the image intensity levels range from 0 to 1155. The bias-corrected versions by GP, WD, and NEW3 of the denoised image by TV in the case with 3% Rician noise are shown in the first row of Figure 12. The corresponding deviation images are shown in the second row of the figure, from which it seems that the deviation image by NEW3 has the weakest pattern.

We then repeated the simulation 100 times. Table 5 presents the estimated MISE values and

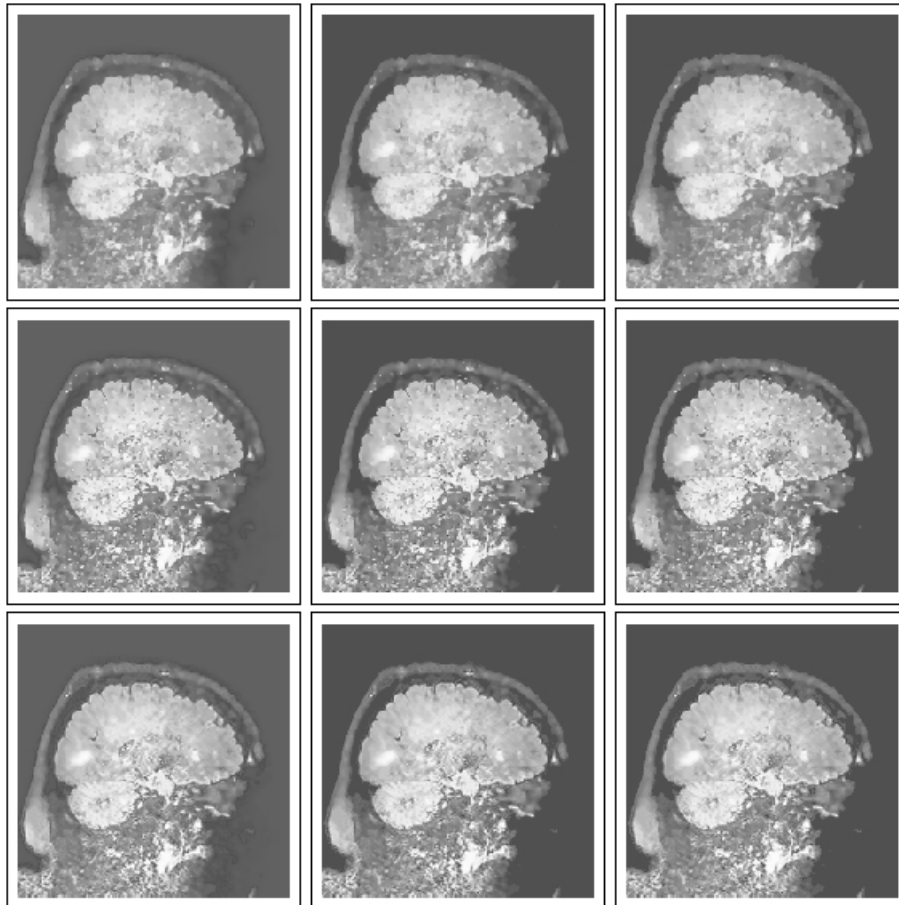


Figure 10: Bias-corrected denoised images in the real noisy MRI image example. Rows 1-3 presents the denoised images by denoising procedures TV, AD and ONLM. Columns 1-3 presents the bias-corrected denoised images by procedures GP, WD and NEW3.

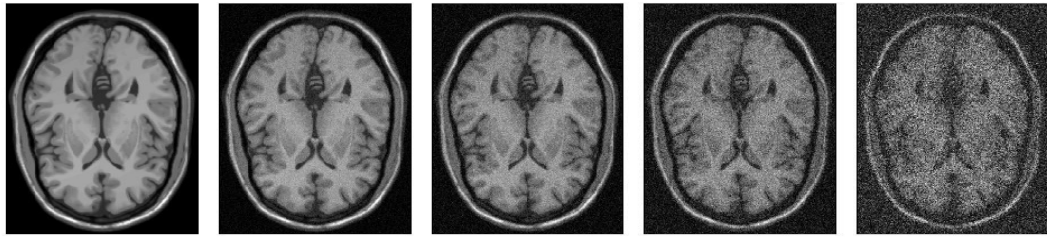


Figure 11: A noiseless brain phantom image with 40% intensity non-uniformity (1st panel), and its four noisy versions with 3% (2nd panel), 5% (3rd panel), 9% (4th panel), and 20% (5th panel) Rician noise.

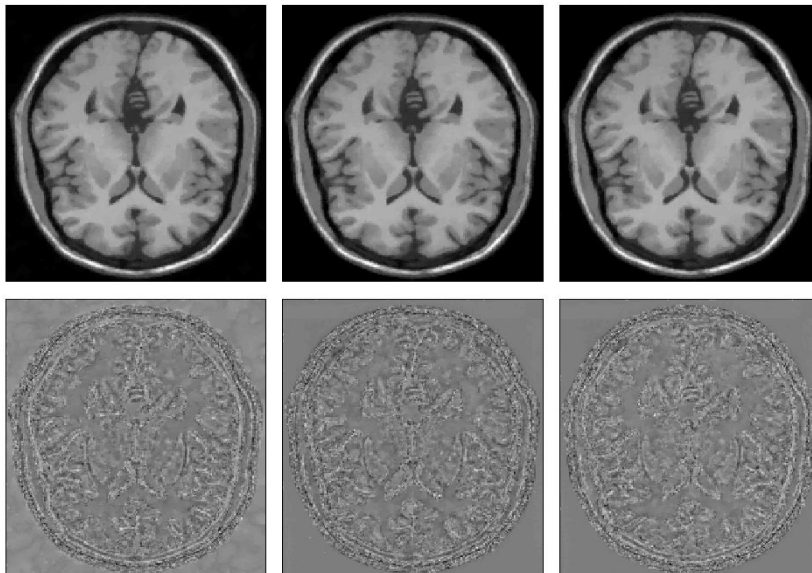


Figure 12: Images in the first row show the three bias-corrected versions by GP, WD, and NEW3 of the denoised image by TV in the case when the observed image is the one shown in the 2nd panel of Figure 11 with 3% Rician noise. Images in the second row show the corresponding deviation images.

their standard errors, the estimated ABIAS values, and the estimated trimmed contrasts and their standard errors. It can be seen from the table that NEW3 uniformly outperforms GP and WD in terms of both ABIAS and the trimmed contrast. In terms of MISE, NEW3 outperforms GP in all cases, it outperforms WD when the noise level is 3% and 20%, and it is slightly worse than WD when the noise level is 5% and 9%.

## 4 Conclusions

We have presented a bias-correction method for removing the bias caused by the Rician noise that is commonly seen in observed MRI images. Our method is based on a direct expression of the estimation bias using the function  $f_1$ , and on a Monte Carlo approximation to its inverse function  $g_1$  (cf., formulas (5)–(8)). An explicit formula for approximating the function  $g_1$  is also provided, using the first-order regression spline smoothing. Therefore, its bias-corrected denoised image  $\hat{m}(x, y)$  in (8) can be easily computed. Numerical studies show that it performs well in applications, compared to its peers GP and WD (cf., the formulas (3) and (4)).

**Acknowledgments:** The authors thank the associate editor and four referees for many constructive comments and suggestions which greatly improved the quality of the paper. This research is supported in part by an NSF grant.

Table 5: Performance of the bias-correction methods GP, WD, and NEW3 on the denoised images by TV when the experiments are done on the brain phantom image with 40% intensity non-uniformity and noise levels of 3%, 5%, 9%, and 20%. In each entry, the first row presents the estimated MISE value and its standard error (in parenthesis), the second row presents the estimated ABIAS value, and the third row presents the estimated trimmed contrast and its standard error. All results are based on 100 replicated simulations.

	GP	WD	NEW3
3% Rician noise	473.0 (20.0)	426.6 (11.8)	417.7 (6.9)
	11.1	8.4	7.6
	784.5 (3.3)	788.7 (2.9)	790.8 (2.9)
5% Rician noise	1226.7 (64.0)	855.3 (12.9)	859.6 (13.7)
	20.4	11.4	10.5
	764.6 (5.9)	783.0 (2.8)	788.7 (2.9)
9% Rician noise	5980.4 (173.5)	1944.7 (36.4)	1967.8 (33.1)
	59.2	19.7	17.8
	673.6 (7.6)	774.9 (3.6)	781.4 (3.9)
20% Rician noise	14369.0 (700.7)	6813.7 (498.3)	6094.2 (223.2)
	86.4	48.5	33.9
	649.7 (14.9)	739.2 (8.4)	772.0 (7.9)

## REFERENCES

1. Vlaardingerbroek MT, den Boer JA. *Magnetic Resonance Imaging (2nd ed.)* 1999; New York: Springer-Verlag.
2. Qiu P. *Image Processing and Jump Regression Analysis*. 2005; New York: John Wiley & Sons.
3. Gudbjartsson H, Patz, S. The noisy distribution of noisy MRI data. *Magnetic Resonance in Medicine* 1995; **34**:910–915.
4. Macovski A. (1996). Noise in MRI. *Magnetic Resonance in Medicine* 1996; **36**:494–497.
5. Bernstein MA, Thomasson DM, Perman WH. Improved detectability in low SNR MR images by means of phase-corrected real construction. *IEEE Transactions on Image Processing* 1989; **16**:813–817.
6. Sijbers J, den Dekker AJ, Scheunders P, Dyck DV. Maximum-likelihood estimation of Rician distribution parameters. *IEEE Transactions on Medical Imaging* 1998; **17**:357–361.
7. Nowak R. Wavelet-Based Rician Noise Removal for Magnetic Resonance Imaging. *IEEE Transactions on Image Processing* 1999; **8**:1408–1419.
8. Haacke EM, Brown RW, Thompson MR, Venkatesan R. *Magnetic Resonance Imaging: Physical Principles and Sequence Design* 1999; New York: John Wiley & Sons.
9. Rudin L, Osher S, Fatemi E. Nonlinear total variation based noise removal algorithms. *Physica D* 1992; **60**:259–268.
10. Perona P, Malik J. Scale-space and edge detection using anisotropic diffusion *IEEE Transactions on Pattern Analysis and Machine Intelligence* 1990; **12**:526–556.

11. Buades B, Coll B, Morel JM. A non-local algorithm for image denoising. *IEEE CVPR* 2005; 60–65.
12. Gijbels I, Lambert A, Qiu P. Edge-preserving image denoising and estimation of discontinuous surfaces. *IEEE Transactions on Pattern Analysis and Machine Intelligence* 2006; **28**:1075–1087.
13. Qiu P, Mukherjee PS. Edge structure preserving image denoising. *Signal Processing* 2010; **90**:2851–2862.
14. Kristoffersen A. Optimal estimation of the diffusion coefficient from non-averaged and averaged noisy magnitude data. *Journal of Magnetic Resonance* 2007; **187**:293–305.
15. Zhu HT, Li Y, Ibrahim JG, Shi X, An H, Chen Y, Gao W, Lin W, Rowe DB, Peterson BS. Regression models for identifying noise sources in magnetic resonance images. *Journal of American Statistical Association* 2009; **104**:623–637.
16. Sijbers J, den Dekker AJ. Maximum likelihood estimation of signal amplitude and noise variance from MR data. *Magnetic Resonance in Medicine* 2004; **51**:586–594.
17. Aja-Fernández S, Alberola-López C, Westin CF. Noise and signal estimation in magnitude MRI and Rician distributed images: A LMMSE approach. *IEEE Transactions on Image Processing* 2008; **17**(8):1383–1398.
18. Coupé P, Manjon JV, Gedamu E, Arnold D, Robles M, Collins DL. Robust Rician noise estimation for MR images. *Medical Image Analysis* 2010; **14**(5):483–493.
19. Rajan J, Poot D, Juntu J, Sijbers J. Noise measurement from magnitude MRI using local estimates of variance and skewness. *Physics in Medicine and Biology* 2010; **55**:441–449.

20. Coupé P, Yger P, Prima S, Hellier P, Kervrann C, Barillot C. An optimized blockwise nonlocal means denoising filter for 3-D magnetic resonance images. *IEEE Transactions on Medical Imaging* 2008; **27**:425–441.
21. Wiest-Daessle N, Prima S, Coupe P, Morrissey S, Barillot C. Rician noise removal by non-Local Means filtering for low signal-to-noise ratio MRI: Application to DT-MRI. *MICCAI, New York/USA* 2008; 104–117.
22. Chung KL. *A Course In Probability Theory (2nd ed.)* 1974; New York: Academic Press, Inc.
23. Getreuer P. tvdenoise.m (a MATLAB program) 2008; <http://www.mathworks.nl/matlabcentral/fileexchange/16236>.
24. Lopes DS. anisodiff3D.m (a MATLAB program) 2007; <http://www.mathworks.co.uk/matlabcentral/fileexchange/14995-anisotropic-diffusion-perona-malik>.
25. Marjón JV, Coupé P, Marti-Bonmatí L, Collins DL, Robles M. Adaptive non-local means denoising of MR images with spatially varying noise levels. *Journal of Magnetic Resonance Imaging* 2010; **31**:192–203.
26. <http://www.bic.mni.mcgill.ca/brainweb/>
27. Cocosco CA, Kollokian V, Kwan RK-S, Evans AC. BrainWeb: Online Interface to a 3D MRI Simulated Brain Database. *NeuroImage* 1997; **5**(4): part 2/4, S425, 1997 – *Proceedings of 3-rd International Conference on Functional Mapping of the Human Brain*; Copenhagen, May 1997.
28. Kwan RK-S, Evans AC, Pike GB. MRI simulation-based evaluation of image-processing and classification methods. *IEEE Transactions on Medical Imaging* 1999; **18**(11):1085–1097.

29. Kwan RK-S, Evans AC, Pike GB. An Extensible MRI Simulator for Post-Processing Evaluation. *Visualization in Biomedical Computing 1996; Lecture Notes in Computer Science*, **1131**:135–140. Springer-Verlag.
30. Collins DL, Zijdenbos AP, Kollokian V, Sled JG, Kabani NJ, Holmes CJ, Evans AC. Design and Construction of a Realistic Digital Brain Phantom. *IEEE Transactions on Medical Imaging* 1998; **17**(3):463–468.